

Calibrated Simplex Mapping Classification

Raoul Heese^{1,2,*}, Michał Walczak^{1,2}, Michael Bortz^{1,2} and Jochen Schmid²

¹Fraunhofer Center for Machine Learning

²Fraunhofer ITWM, Optimization Department,
Fraunhofer-Platz 1, 67663 Kaiserslautern, Germany

*raoul.heese@itwm.fraunhofer.de

December 27, 2021

Abstract

We propose a novel supervised multi-class/single-label classifier that maps training data onto a linearly separable latent space with a simplex-like geometry. This approach allows us to transform the classification problem into a well-defined regression problem. For its solution we can choose suitable distance metrics in feature space and regression models predicting latent space coordinates. A benchmark on various artificial and real-world data sets is used to demonstrate the calibration qualities and prediction performance of our classifier.

1 Introduction

In many supervised learning applications, it is not sufficient to know the most probable class y for a certain data point x . Instead, a well-calibrated probabilistic prediction $p(y|x)$ is required. For instance, in clinical applications, class probabilities are important for confidence in model predictions (Challis et al., 2015). Some classifiers intrinsically provide such a posterior probability, e. g. logistic regression or Gaussian process classification (GPC) as described in Rasmussen and Williams (2006). There are also various methods to install or improve such a calibration for a given classification approach (Niculescu-Mizil and Caruana, 2005), like Platt scaling (Platt, 2000) or isotonic regression (Zadrozny and Elkan, 2002).

A binary GPC algorithm with classes $y \in \{-1, +1\}$ consists of three steps, as outlined in Rasmussen and Williams (2006): First, a latent function $f(x)$ with a GP prior is defined. Second, the distribution of the latent variable corresponding to a test case is determined. And third, this distribution times the sigmoid function of the latent variable $\sigma(f)$ is integrated over to determine the probabilistic prediction $p(y = +1|x)$. Since it is effectively integrated out, the latent function, practically, only aids in the convenient formulation of the model. However, the latent function could potentially be used to decide whether a point corresponds to class $+1$ ($f(x) > 0$) or class -1 ($f(x) < 0$). In other words, $f(x)$ indicates the degree of membership of a point x to each class. This degree of membership arises purely from the data statistics.

The exact calculation of $p(y = +1|x)$ might be time-consuming or even intractable, and its approximation inaccurate. To address these limitations, we propose a different approach, which is based on a distance-based latent function $f(x)$. Specifically, our approach is two-fold. First, we determine

$$f(x) \equiv \text{closest distance of } x \text{ to a point of the opposite class} \quad (1)$$

for each training point x . Second, we train a suitable regression model to learn this mapping, for example a Gaussian process regressor (GPR), see Rasmussen and Williams (2006). The prediction of this model then allows us to determine $p(y = +1|x)$ analytically. Our approach can be extended to multi-class problems by mapping the distance-based features onto a simplex-like geometry. Hence, we name it *calibrated simplex mapping classifier* or *CASIMAC*.

In Figure 1 we show a simple one-dimensional classification problem to illustrate the connection between latent functions, probabilities and the training data for our proposed method and a GPC. To reduce the computational effort, the GPC predictions are usually approximated. To this end, several approaches, e. g.

the Laplace method, the expectation propagation method (Rasmussen and Williams, 2006), the variational inference method (Tran et al., 2015) or the Markov chain Monte-Carlo method (Hensman et al., 2015) are typically used, just to name a few. However, these approximations may lead to counter-intuitive probabilities which do not reflect a well-calibrated model despite their possibly good classification accuracy (Rasmussen and Williams, 2006). In our example in Figure 1 we clearly see that there are regions of densely sampled data points of a single class, which the GPC probabilities judge as uncertain. In contrast, our CASIMAC method has a very high confidence for such regions as one would intuitively expect. This is because we have based our latent function $f(x)$ on the actual locations of the data points, Eq. (1). Furthermore, we do not require any approximations for the calculation of the class probabilities.

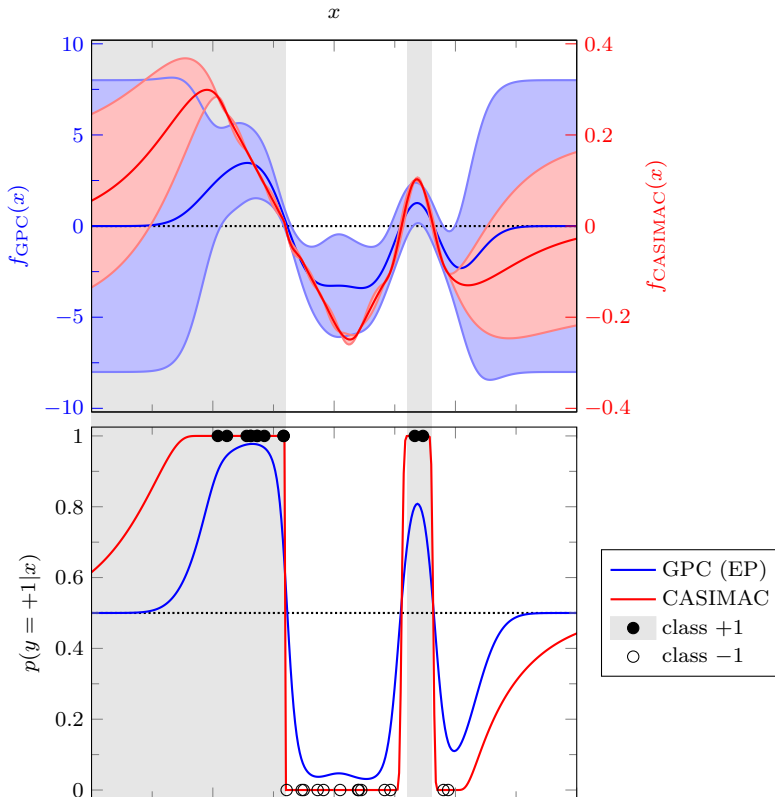


Figure 1: Binary classification problem with a one-dimensional continuous feature x and a class label $y \in \{-1, +1\}$. We compare GPC (using an RBF kernel and expectation propagation (EP) with the implementation from GPy, 2012) and our proposed CASIMAC method (based on a GPR with Matern kernel) both trained on the same 25 training data points. The top plot shows the expectation values and the standard deviations of the latent functions $f(x)$ for both approaches (on two different scales), whereas the bottom plot contains the probabilistic prediction of class membership $p(y = +1|x)$ for both approaches. The horizontal lines (-----) represent the respective decision boundaries. Grey areas correspond to the true regions of class +1; the data is sampled without noise. It is clearly visible from the bottom plot that the CASIMAC prediction has a much higher confidence at or near the training data points and therefore appears more intuitive than the GPC prediction. Furthermore, the CASIMAC predictions were calculated without any approximations.

Summarized, our approach transforms a classification problem into a regression problem: Instead of a class label, we predict the latent space position of a feature space point. Due to the latent space structure, we can uniquely infer the corresponding class label from this position. This approach allows a very generic treatment of classification problems and enables us to choose suitable distance metrics and regression models.

The concept of leveraging Bayesian probabilistic prediction power combined with latent space mapping has been studied before. Several recent publications propose to couple a deep neural network with Gaussian

processes (GP) for an improved uncertainty estimate of model predictions (Calandra et al., 2016; Wilson et al., 2016; Al-Shehivat et al., 2017; Bradshaw et al., 2017; Daskalakis et al., 2020). Alternative approaches explore the use of deep neural networks not as feature extraction methods but, for instance, to suitably estimate the mean functions of GPs (Iwata and Ghahramani, 2017) or to predict their covariance functions and hyper-parameters (Cremanns and Roos, 2017). However, due to high complexity of the deep neural network components in these models, the algorithms mentioned above are well suited for large data sets with abundant training data available (Liu et al., 2018). By contrast, in this paper, we propose a simple latent space mapping as a core component of a well calibrated classifier that also works on less complex data sets. Our method has recently been successfully used for an industrial application (Ludl et al., 2021).

The paper is organized as follows. In Section 2, we introduce our CASIMAC method. In Section 3 we compare our classifier with other approaches on different data sets. Finally, we conclude with a summary and outlook in Section 4.

2 Proposed Method

We consider a multi-class/single-label classification problem with a d -dimensional feature space $\mathcal{X} \subseteq \mathbb{R}^d$ and $n \geq 2$ different classes $\mathcal{Y} \equiv \{1, \dots, n\} \subset \mathbb{Z}$. The training data set

$$\mathbf{D} \equiv \{(\mathbf{x}_1, y_1), \dots, (\mathbf{x}_D, y_D)\} \in \mathcal{D} \quad (2)$$

consists of D data points $\mathbf{d} \equiv (\mathbf{x}, y)$ with $\mathbf{x} \in \mathcal{X}$ and $y \in \mathcal{Y}$. We denote the respective data space with $\mathcal{D} \equiv (\mathcal{X} \times \mathcal{Y})^D$.

Performing a classification task for such a problem with our CASIMAC method first requires a training stage, which is based on two steps:

- (t1) Map the training data to a linearly separable latent space.
- (t2) Train a regression model for this mapping.

After the training has been performed, predictions are made using again a two-step approach:

- (p1) Predict the latent space position of a query point using the previously trained regression model.
- (p2) Map the latent space position to its corresponding class.

We illustrate this strategy in Figure 2 for a simple example with three classes and a two-dimensional feature space. The predicted class border is shown in the left panel in Figure 2a.

In the following, we explain our approach in more detail. Specifically, we first define the latent space mapping—necessary for step (t1)—and its inversion—necessary for step (p2)—in Section 2.1. In Section 2.2 we discuss the regression model, which is required for step (t2) and step (p1), and describe how we can use it to predict class labels. If the regression model also provides a probabilistic prediction, we can use it to make a probabilistic prediction of class labels as shown in Section 2.3. Finally, we discuss in Section 2.4 how our approach can also be used for visualization purposes.

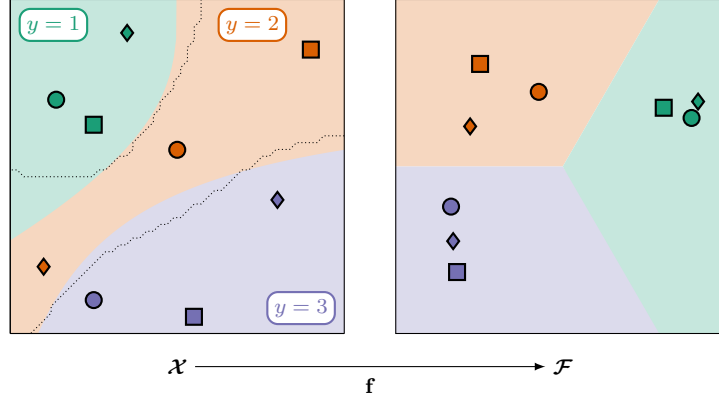
2.1 Latent Space Mapping

In step (t1) of our method, we perform a mapping

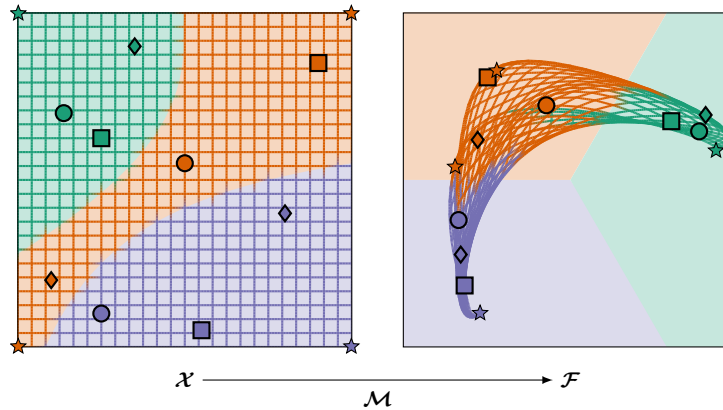
$$\mathbf{f} : \mathcal{D} \times \mathcal{X} \times \mathcal{Y} \mapsto \mathcal{F} \quad (3)$$

from the joint domain of data space \mathcal{D} , feature space \mathcal{X} and class labels \mathcal{Y} to a $(n - 1)$ -dimensional latent space $\mathcal{F} \equiv \mathbb{R}^{n-1}$. We have already motivated a simple example for such a mapping in Eq. (1), which we generalize in the following. In particular, we propose

$$\mathbf{f}_{\alpha, \beta, k_\alpha, k_\beta}(\mathbf{D}, \mathbf{x}, y) \equiv - \sum_{\substack{y'=1 \\ y' \neq y}}^n C_{\alpha, \beta, k_\alpha, k_\beta}(\mathbf{D}, \mathbf{x}, y, y') \mathbf{p}_{y'}, \quad (4)$$



(a) Step (t1): Transform the training data with \mathbf{f} , Eq. (3), by mapping it from the feature space \mathcal{X} to a latent space \mathcal{F} on a $(n-1)$ -simplex-like geometry, where $n=3$ is the number of classes. Here we use an euclidean distance metric with the parameters $\alpha=0$ and $\beta=k_\beta=1$, Eq. (6). In \mathcal{F} , all points are linearly separable with respect to the origin. In the left panel we also show the resulting predicted class borders (.....) based on $\hat{y}(\mathbf{x}|\mathbf{D})$, Eq. (14). The prediction accuracy on the training data set is 100%.



(b) Step (t2): Train a regression model \mathcal{M} , Eq. (11), on the data from step (t1) to map from the feature space \mathcal{X} to the latent space \mathcal{F} . To illustrate the mapping, we show a grid in the feature space and its transformation to the latent space by the estimator. This grid is “pinned” by the sampled points so that the purpose of the estimator is to interpolate grid deformation in-between the points and extrapolate it beyond them. For reference, we also show the mapping of the grid edges (\star). The estimator we use here is a GPR with Matern kernel.

Figure 2: Ternary classification problem with two-dimensional features to illustrate the two training steps of our proposed CASIMAC method; c.f. Section 2. The colored regions illustrate the true regions of the three classes (with the respective labels), whereas the points denote the (noiselessly) sampled training data \mathbf{D} , Eq. (2). We sample three points from each class and use different symbols (\circ , \square and \diamond) to uniquely identify each point.

which represents a decomposition into the vectors $\mathbf{p}_i \in \mathbb{R}^{n-1} \forall i=1, \dots, n$. These n vectors are defined as the affinely independent vertices of a regular $(n-1)$ -simplex with barycenter $\mathbf{0} \in \mathbb{R}^{n-1}$ (Coxeter, 1973; Boyd and Vandenberghe, 2004). One has

$$\sum_{i=1}^n \mathbf{p}_i = \mathbf{0} \tag{5a}$$

and

$$\|\mathbf{p}_i\|_2 = \|\mathbf{p}_j\|_2 \forall i, j = 1, \dots, n, \tag{5b}$$

respectively, where $\|\cdot\|_2$ denotes the 2-norm. An algorithm to determine the corresponding vertices \mathbf{p}_i is outlined in Appendix B.1.

The coefficients

$$C_{\alpha,\beta,k_\alpha,k_\beta}(\mathbf{D}, \mathbf{x}, y, y') \equiv \alpha \cdot A_{k_\alpha}(\mathbf{D}, \mathbf{x}, y) + \beta \cdot R_{k_\beta}(\mathbf{D}, \mathbf{x}, y') \quad (6)$$

in Eq. (4) consist of a linear combination of two contributions with the user-defined weights $\alpha \in \mathbb{R}_+$ and $\beta \in \mathbb{R}_+$. The first contribution is the so-called attraction

$$A_{k_\alpha}(\mathbf{D}, \mathbf{x}, y) \equiv \frac{1}{\text{NN}_{k_\alpha}[\{\mathbf{x}' \in \mathbf{X}(\mathbf{D}, y) : d(\mathbf{x}, \mathbf{x}') > 0\}]} > 0 \quad (7a)$$

and the second contribution is the so-called repulsion

$$R_{k_\beta}(\mathbf{D}, \mathbf{x}, y) \equiv \text{NN}_{k_\beta}[\mathbf{X}(\mathbf{D}, y)] \geq 0. \quad (7b)$$

Here we have introduced the mean distance

$$\text{NN}_k[\mathbf{X}] \equiv \frac{1}{k} \min_{\substack{\mathbf{X}' \subseteq \mathbf{X} \\ |\mathbf{X}'|=k}} \sum_{\mathbf{x}' \in \mathbf{X}'} d(\mathbf{x}, \mathbf{x}') \quad (8)$$

of the k nearest neighbors

$$\mathbf{X}(\mathbf{D}, y) \equiv \{\mathbf{x}' \in \mathcal{X} : (\mathbf{x}', y') \in \mathbf{D} \wedge y' = y\}$$

of a certain class y with respect to a given distance metric

$$d : \mathcal{X} \times \mathcal{X} \mapsto \mathbb{R}_{\geq 0} \quad (9)$$

on \mathcal{X} . In particular, this distance metric can be chosen to fit the problem at hand (Deza and Deza, 2016). For the attractions, Eq. (7a), we filter out all neighbors with vanishing distances to avoid a division by zero. We explain the motivation behind the attraction and repulsion coefficients further below. The number of nearest neighbors $k_\alpha \in \mathbb{N}_{\geq 1}$ and $k_\beta \in \mathbb{N}_{\geq 1}$, respectively, are also user-defined parameters. For reasons of clarity, all user-defined parameters are written as superscripts.

Note that Eq. (1) represents a simplification of Eq. (4) with $\alpha = 0$ and $\beta = k_\beta = 1$. We present a slight generalization of Eq. (4) in Appendix B.2, which we have used for our implementation.

By definition, $C_{\alpha,\beta,k_\alpha,k_\beta}(\mathbf{D}, \mathbf{x}, y, y')$ is not bounded, hence the mapping is not limited to the interior of the unit simplex, but can reach the entire \mathbb{R}^{n-1} . However, the resulting geometry can still be considered as an infinitely large simplex-like shape. In particular, due to this geometry the proposed mapping allows a linear separability of all classes with respect to the origin in \mathcal{F} . In other words, there exists a well-defined mapping back onto the class labels

$$y : \mathcal{F} \mapsto \mathcal{Y}$$

given by

$$y(\mathbf{f}) = \min_{y \in \mathcal{Y}} \|\mathbf{f} - \mathbf{p}_y\|_2^2, \quad (10)$$

which allows a flawless class reconstruction. As explained further below, this reconstruction is important to make predictions. Since it is a central aspect of our proposed method, we sketch a proof of Eq. (10) in Appendix A.

To demonstrate the linear class separability in a more intuitive way, we recall our initial example from Figure 2 and show the corresponding simplex vertices \mathbf{p}_1 , \mathbf{p}_2 , and \mathbf{p}_3 in Figure 3. Each vertex is associated with one class (as indicated by the colors and the respective labels) and allows a linear separation from the origin $\mathbf{0}$ along the vertices $-\mathbf{p}_1$, $-\mathbf{p}_2$, and $-\mathbf{p}_3$, which span the origin mirrored simplex. As defined by Eq. (4), a data point of class y is mapped onto the latent space as a superposition of the vertices $-\mathbf{p}_{y' \neq y}$ with positive coefficients. Thus, it is clear from Figure 3 that it is always mapped into the correct region y

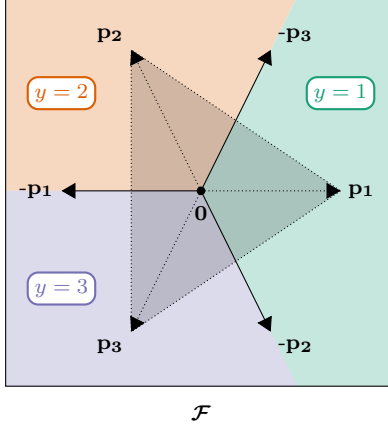


Figure 3: Latent space \mathcal{F} for the ternary classification problem from Figure 2. Its geometry can be understood as an infinitely stretched regular 2-simplex defined by the vertices \mathbf{p}_1 , \mathbf{p}_2 , and \mathbf{p}_3 and the barycenter $\mathbf{0}$ (shown as a shaded triangle). The latent space can be segmented into three congruent shapes, each associated with one of the three classes as indicated by the respective colors and labels $y = 1, 2, 3$. The class borders stretch from the origin $\mathbf{0}$ along the vertices of the mirrored simplex $-\mathbf{p}_1$, $-\mathbf{p}_2$ and $-\mathbf{p}_3$, respectively.

(or on its border for vanishing coefficients), which can be identified using Eq. (10). This also holds true for higher-dimensional simplices.

Based on these considerations, the motivation behind the attraction and repulsion coefficients, Eq. (7), respectively, can be made clear. For this purpose we rewrite Eq. (4) as

$$\mathbf{f}_{\alpha, \beta, k_\alpha, k_\beta}(\mathbf{D}, \mathbf{x}, y) \equiv \alpha \cdot A_{k_\alpha}(\mathbf{D}, \mathbf{x}, y) \mathbf{p}_y - \sum_{\substack{y'=1, \dots, n \\ y' \neq y}} \beta \cdot R_{k_\beta}(\mathbf{D}, \mathbf{x}, y') \mathbf{p}_{y'}$$

using Eqs. (5a) and (6). Thus, we find that for a data points of class y the attraction term points in the direction of \mathbf{p}_y , whereas the repulsion term points into the opposite directions of the remaining vertices. This means that a data point with a smaller distance to neighbors of the same class in the feature space (resulting in a higher attraction term) pushes the corresponding latent point further into the region of its class. Similarly, a higher distance of the data point to neighbors of the opposite class (resulting in a higher repulsion term) pushes the corresponding latent point further away from the region of this opposite class (and hence closer to the own region). In other words, each training data point is mapped onto a simplex segment corresponding to its class with a position reflecting its inter-class distances.

This generic behavior can be customized in many ways with our approach. First, the user-defined parameters α , β , k_α , and k_β can be used to tune the behavior and influence of attraction and repulsion in Eq. (4). Second, since these coefficients are based on a distance metric $d(\cdot, \cdot)$, this metric can be adjusted to the problem at hand. And, lastly, the choice of the model is crucial for step (t2) and step (p1) of the classification process. We discuss this aspect in more detail in the following.

2.2 Regression Model

In step (t2) of our proposed method, we train a regression model

$$\mathcal{M} : \mathcal{X} \rightarrow \mathcal{F} \tag{11}$$

to predict points in the latent space \mathcal{F} from points in the feature space \mathcal{X} . For this purpose, we define the feature data set

$$\mathbf{D}_F \equiv \{(\mathbf{x}_1, \mathbf{f}_1), \dots, (\mathbf{x}_D, \mathbf{f}_D)\} \in \mathcal{D}_F \tag{12}$$

based on the training data set \mathbf{D} , Eq. (2), with

$$\mathbf{D}_{\mathbf{F}} = \{(\mathbf{x}, \mathbf{f}) \in \mathcal{X} \times \mathcal{F} : (\mathbf{x}, y) \in \mathbf{D}, \mathbf{f} = \mathbf{f}_{\alpha, \beta, k_{\alpha}, k_{\beta}}(\mathbf{D} \setminus \{(\mathbf{x}, y)\}, \mathbf{x}, y)\} \quad (13)$$

and denote the respective feature data space as $\mathcal{D}_{\mathcal{F}} \equiv (\mathcal{X} \times \mathcal{F})^D$.

Specifically, the model \mathcal{M} is trained on $\mathbf{D}_{\mathbf{F}}$. Its predictions $\hat{\mathbf{f}}(\mathbf{x}|\mathbf{D})$ serve as an estimate for the simplex feature mapping, Eq. (3), without having knowledge about the class of the queried point in the sense of

$$\mathcal{D} \times \mathcal{X} \mapsto \mathcal{F}.$$

By projecting onto the input data subspace of missing class information (c. f. Eq. (3), where \mathcal{Y} is contained in the domain), we intrinsically introduce uncertainty. Additional uncertainty may come from the estimator itself when interpolating or extrapolating missing information or when trying to predict noisy data. However, we put up with these uncertainties to be able to predict class labels purely from the feature space. This is necessary when we want to predict the latent space position of feature space points with an unknown class.

Combining the model prediction with the class reconstruction, Eq. (10), leads to the estimated class

$$\hat{y}(\mathbf{x}|\mathbf{D}) \equiv y(\hat{\mathbf{f}}(\mathbf{x}|\mathbf{D})) \quad (14)$$

which allows us to predict the class of any $\mathbf{x} \in \mathcal{X}$. An example for such a prediction is shown in the left panel of Figure 2a. We emphasize that the inner structure of the estimator \mathcal{M} is completely arbitrary as long as it allows a suitable regression of the form shown in Eq. (11). Hence, the model can be chosen to fit the problem at hand.

2.3 Class Probabilities

If the regression model also provides a probabilistic prediction, we can directly infer the class probabilities. Assume that $\hat{p}(\mathbf{f}|\mathbf{D}, \mathbf{x})$ is the estimated probability density of \mathbf{x} mapping onto \mathbf{f} given \mathbf{D} . Then

$$\hat{p}(y|\mathbf{D}, \mathbf{x}) \equiv \int_{\mathbb{R}^{n-1}} \mathbb{1}(y, \mathbf{f}) \hat{p}(\mathbf{f}|\mathbf{D}, \mathbf{x}) \, d\mathbf{f} \quad (15)$$

is the estimated probability of observing the class $y \in \mathcal{Y}$ for \mathbf{x} given \mathbf{D} . Here we have used the indicator function

$$\mathbb{1}(y, \mathbf{f}) \equiv \begin{cases} 1 & \text{if } y(\mathbf{f}) = y \\ 0 & \text{else} \end{cases} \quad (16)$$

to select the latent space area of the observed class y . If $\hat{p}(\mathbf{f}|\mathbf{D}, \mathbf{x}) \sim \mathcal{N}$ is a normal distribution (as for a GPR), the integral can be solved analytically for $n = 2$. Furthermore, it can also be approximated using Monte-Carlo importance sampling methods for higher dimensions or non-normal distributions. We discuss these approaches in Appendix B.3.

The expected class, Eq. (14), can alternatively also be calculated from

$$\hat{y}(\mathbf{x}|\mathbf{D}) = \sum_{y \in \mathcal{Y}} y \hat{p}(y|\mathbf{D}, \mathbf{x})$$

based on the class probabilities. In Figure 1 we exemplarily show the class probabilities for a binary classification problem using the notation $p(y = +1|x) \equiv \hat{p}(y = +1|\mathbf{D}, \mathbf{x} = (x))$.

2.4 Visualization

The latent space \mathcal{F} can also be used to visualize the properties of a data set. In particular, its dimension is determined by the number of classes n and not the dimensionality d of the feature space \mathcal{X} , which can be useful for high-dimensional data sets with a low number of classes (i. e., $n \ll d$). Specifically, the latent space representation of the data allows to study class relations and can give a hint at how well a separability can be achieved.

For example, in the latent space shown in Figure 2a we find that the distances between samples from the classes 1 or 3 and samples from class 2 are smaller than the distances between samples from the classes 1 and 3 themselves. Clearly, this is because class 2 lies between the classes 1 and 3 in \mathcal{X} . In a higher-dimensional feature space such a relation may, however, be very difficult to see. In such a case the latent space representation will still reveal these inter-class distances regardless of the feature space dimensionality.

By definition, \mathcal{F} is unbound and it might therefore be useful to transform it to a restricted domain for consistent visualization purposes. A very natural approach is to map \mathcal{F} onto a n -dimensional probability simplex \mathcal{S}^n (Boyd and Vandenberghe, 2004). For three classes, an appropriate projection of such a probability simplex corresponds to the interior of the 2-simplex shown in Figure 3 with vertices of unit length. We briefly discuss the bijective transformation

$$\mathcal{F} \longleftrightarrow \mathcal{S}^n \tag{17}$$

in Appendix B.5.

Note that dimensionality reduction methods (Van Der Maaten et al., 2009) can be applied on the latent space (or its corresponding probability simplex space) in the usual way to achieve a lower dimensional representation of the data.

3 Experiments

In this section, we present the performance of our proposed CASIMAC method measured on various data sets. We comment on the implementation of our algorithm in Appendix B. Where not otherwise stated, we have realized our numerical results with the help of scikit-learn (Pedregosa et al., 2011).

First, we demonstrate the performance on a synthetic data set. Second, we use different real-world data sets for which we determine various performance metrics and show an exemplary visualization. Finally, we briefly highlight how the use of a more complex model allows us to perform a classification task with a larger training data set.

3.1 Synthetic Data

We generate a synthetic classification problem with $n = 4$ classes and a two-dimensional feature space $\mathcal{X} \equiv [-1, 1]^2$ (i. e., $d = 2$) based on the rule

$$y_{\text{true}}(\mathbf{x}) \equiv \begin{cases} 1 & \text{if } x_0 > 0 \wedge x_1 > 0 \\ 2 & \text{if } x_0 < 0 \wedge x_1 > 0 \\ 3 & \text{if } x_0 < 0 \wedge x_1 < 0 \\ 4 & \text{if } x_0 > 0 \wedge x_1 < 0 \end{cases} \tag{18}$$

for features $\mathbf{x} \equiv (x_0, x_1) \in \mathcal{X}$. The problem is illustrated in Figure 4. In particular, the synthetic data is free of noise.

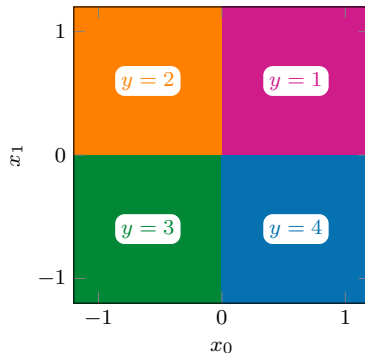


Figure 4: Illustration of the synthetic data set ground truth labels as defined in Eq. (18).

The training data set, Eq. (2), consists of $D = 40$ points sampled uniformly from \mathcal{X} . Analogously, the test data set

$$\mathbf{T} \equiv \{(\mathbf{x}_1, y_1), \dots, (\mathbf{x}_T, y_T)\} \in \mathcal{D}$$

consists of $T = 10\,000$ uniformly sampled points. Here and in the following, we always standardize the features based on the training data before feeding it to the classifiers.

For our CASIMAC algorithm described in Section 2, we parameterize the weights for the attraction and repulsion coefficients, Eq. (7), by a single parameter $\gamma \in [0, 1]$ with

$$\gamma = \beta = 1 - \alpha \tag{19}$$

so that $\alpha, \beta \in [0, 1]$. As distance metric, Eq. (9), we use the 2-norm (Euclidean norm)

$$d_2(\mathbf{x}_1, \mathbf{x}_2) \equiv \|\mathbf{x}_1 - \mathbf{x}_2\|_2 \tag{20}$$

for all $\mathbf{x}_1, \mathbf{x}_2 \in \mathcal{X}$. For the regression model, Eq. (11), we choose a GPR with a combination of a Matern and a white noise kernel (Rasmussen and Williams, 2006). We compare our classifier with a (one-versus-rest) GPC with the same kernel. The hyper-parameters of both estimators are tuned by cross-validating the training data over a predefined set of different setups as outlined in Appendix C.

In total, we perform 10 classification tasks, each with different test and training data sets. For each, we use the test data set to determine the accuracy (fraction of correctly predicted points) and the log-loss (i. e., the logistic regression loss or cross-entropy loss). Furthermore, we calculate the proba-loss, which is defined as the mean predicted probability error

$$\delta p \equiv 1 - \frac{1}{T} \sum_{i=1}^T \hat{p}(y = y_{\text{true}}(\mathbf{x}_i) | \mathbf{D}, \mathbf{x}_i), \tag{21}$$

where $\hat{p}(y | \mathbf{D}, \mathbf{x})$, Eq. (15), denotes the predicted class probability. One has $\delta p \in [0, 1]$ with 0 being the best possible outcome and 1 the worst. This score can only be computed because we know the underlying rule of the problem, Eq. (18).

The results are shown in Table 1. Clearly, our method has a better proba-loss and log-loss in comparison with the GPC, whereas the latter has a slightly better accuracy.

Table 1: Test scores for the synthetic data set based on $T = 10\,000$ uniformly sampled test data points. The proba-loss is defined in Eq. (21). We show the means and the corresponding standard deviations (in brackets) over all 10 classification tasks. The best mean results are highlighted in bold.

Score	CASIMAC	GPC
proba-loss	0.106(14)	0.552(26)
log-loss	0.406(332)	0.825(55)
accuracy	0.913(17)	0.924(18)

We also show an exemplary visualization of the predicted class probabilities in Figure 5 for a single training data set. The background colors represent a weighted average of the class colors from Figure 4 with a weight corresponding to the predicted probability of the respective class. Hence, for a perfectly calibrated prediction, the colors in Figure 5 would correspond to the colors in Figure 4. Although our CASIMAC has a slightly lower training accuracy than the GPC (0.925 instead of 1.000), it clearly exhibits brighter, more distinguishable colors. This means, the predicted probabilities are less uniform and correspond more clearly to a decision for one of the four classes instead of an uncertain mixture. This observation corresponds to the lower proba-loss and log-loss results in Table 1.

3.2 Real-world Data

In the following, we consider five real-world data sets from different fields. An overview is shown in Table 2. All of these data sets are publicly available online.

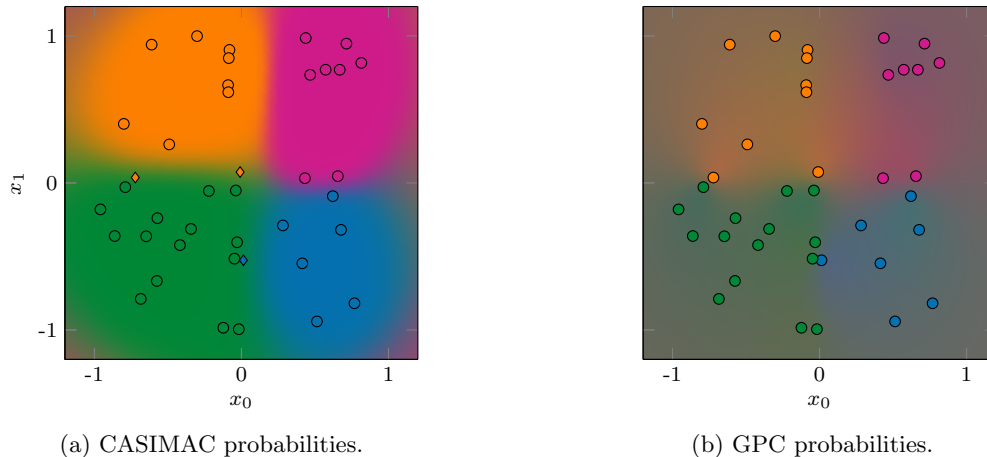


Figure 5: Predictions of the class probabilities for the synthetic data set. The color of each background point corresponds to the weighted average of the class colors from Figure 4 with a weight corresponding to the predicted probability of the respective class at this point. Thus, clear colors as in (a) represent high probabilities for a single class, whereas washed-out colors as in (b) represent almost uniform probabilities. We also show the corresponding training data set (consisting of $D = 40$ points) on which the classifiers have been trained. The color of the points corresponds to their true class. Most of the training data points are correctly classified (shown as \circ), but our CASIMAC incorrectly predicts three training data points (shown as \diamond) close to the class borders.

Table 2: Overview of the five real-world data sets. Shown are the number of classes n , the number of features d , the total number of data points I and the number of training data points D . The number of test data points T can be inferred from $T \equiv I - D$. We abbreviate the references as a) Dua and Graff (2017), b) Adak et al. (2019), c) Lucas et al. (2013), d) Rögvaldsson et al. (2014), e) Baumgardner et al. (2015), f) Graña and M. A. Veganzons (2014), g) Niculescu-Mizil and Caruana (2005), and h) Rohra et al. (2016). Note that we turn the originally multi-class data set `pine` into a binary problem as described in Niculescu-Mizil and Caruana (2005).

Name	n	d	I	D	Refs.
<code>alcohol</code>	5	10	125	50	a), b)
<code>climate</code>	2	18	540	50	a), c)
<code>hiv</code>	2	160	6 590	125	a), d)
<code>pine</code>	2	200	21 025	2 000	e), f), g)
<code>wifi</code>	4	7	2 000	500	a), h)

Additional to the previously introduced GPC, we also compare our proposed algorithm with an artificial neural network with fully-connected layers (MLP) and a k -nearest neighbor classifier (kNN). This classifier choice was dictated by their reported good performance in yielding well-calibrated predictions (Niculescu-Mizil and Caruana, 2005). Again, we tune the hyper-parameters of the estimators by cross-validation as outlined in Appendix C. As distance metric, Eq. (9), we use the 2-norm, Eq. (20), for all data sets except for the `wifi` data set for which the 1-norm (taxicab norm)

$$d_1(\mathbf{x}_1, \mathbf{x}_2) \equiv \|\mathbf{x}_1 - \mathbf{x}_2\|_1$$

for all $\mathbf{x}_1, \mathbf{x}_2 \in \mathcal{X}$ leads to a better performance.

The test-training split of the data is performed by means of a stratified random sampling with respect to the class labels. Average test scores over 10 classification tasks with different training data sets are reported in Table 3. Note that for multi-class data sets, the f1 score is calculated as the weighted arithmetic mean over

harmonic means (Opitz and Burst, 2019), where the weight is determined by the number of true instances for each class. Analogously, we calculate the precision score (ratio of true positives to the sum of true positives and false positives) and recall score (ratio of true positives to the sum of true positives and false negatives) as weighted averages over all classes.

Table 3: Test scores for the benchmarked classifiers on the five real-world data sets from Table 2. We show the means and the corresponding standard deviations (in brackets) over all 10 classification tasks. The best mean results are highlighted in bold.

Score	CASIMAC	GPC	kNN	MLP
alcohol				
accuracy	0.907(62)	0.897(44)	0.545(88)	0.848(47)
f1	0.901(67)	0.894(48)	0.526(93)	0.845(53)
precision	0.928(44)	0.922(30)	0.556(106)	0.872(43)
recall	0.907(62)	0.897(44)	0.545(88)	0.848(47)
log-loss	0.394(338)	0.932(50)	1.752(1442)	0.755(412)
climate				
accuracy	0.914(2)	0.915(4)	0.915(1)	0.906(12)
f1	0.877(7)	0.879(8)	0.875(2)	0.883(15)
precision	0.854(30)	0.861(30)	0.854(29)	0.874(32)
recall	0.914(2)	0.915(4)	0.915(1)	0.906(12)
log-loss	0.249(17)	0.281(9)	1.060(337)	0.341(48)
hiv				
accuracy	0.902(4)	0.900(5)	0.868(7)	0.880(6)
f1	0.898(5)	0.898(5)	0.862(7)	0.880(6)
precision	0.899(4)	0.898(5)	0.861(7)	0.880(6)
recall	0.902(4)	0.900(5)	0.868(7)	0.880(6)
log-loss	0.263(17)	0.290(7)	0.405(31)	0.404(18)
pine				
accuracy	0.937(1)	0.934(2)	0.916(2)	0.923(5)
f1	0.934(1)	0.931(2)	0.914(3)	0.922(5)
precision	0.933(2)	0.930(2)	0.913(3)	0.922(5)
recall	0.937(1)	0.934(2)	0.916(2)	0.923(5)
log-loss	0.169(7)	0.182(4)	0.396(117)	0.212(43)
wifi				
accuracy	0.977(2)	0.976(2)	0.968(3)	0.969(4)
f1	0.977(2)	0.976(2)	0.969(3)	0.969(4)
precision	0.978(2)	0.977(2)	0.969(3)	0.969(4)
recall	0.977(2)	0.976(2)	0.968(3)	0.969(4)
log-loss	0.130(48)	0.362(48)	0.195(59)	0.093(14)

We find from Table 3 that our CASIMAC exhibits a comparatively good overall score on all data sets considered. In particular, its log-loss is in all cases better than that of the GPC. It is also better than the log-loss of all other classifiers except for the `wifi` data set on which the MLP is superior. Similarly, the accuracy of our approach is also better than that of the other candidates except for the `climate` data set on which GPC and kNN perform slightly better. Taking the uncertainties of the results into account, it turns out that in most cases the scores fall within the range of a single standard deviation of each other. In particular the log-loss, however, shows the most discrepancies between the classifiers.

For binary classification problems, it is also interesting to take a look at the calibration curves (or reliability diagrams) in addition to the scores (DeGroot and Fienberg, 1983; Niculescu-Mizil and Caruana, 2005). For this purpose, we predict the class probabilities of all test samples and discretize the results into ten bins. For each bin, we plot the true fraction of positives against the mean of the corresponding probabilities. For a perfectly calibrated classifier, such a curve corresponds to a diagonal line and deviations from this line can therefore be understood as miscalibrations. Exemplary, we consider the `pine` data set and show a typical calibration curve in Figure 6.

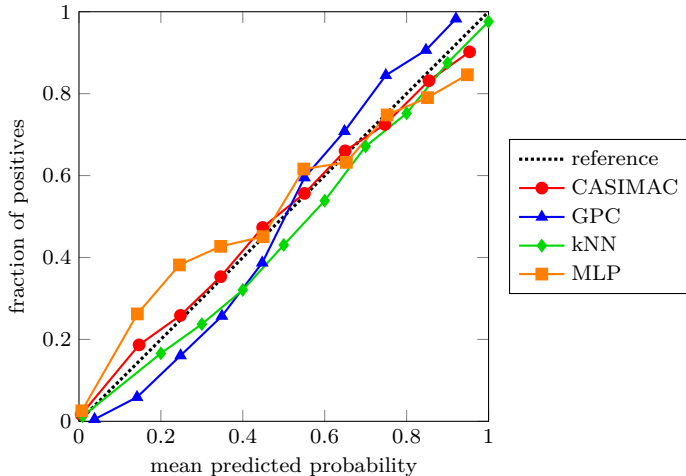


Figure 6: Example calibration curves for the benchmarked classifiers on the `pine` data set. The closer the curves are to the diagonal reference line, the better the calibration of the respective classifier. Our proposed method exhibits the best calibration.

Clearly, the curve of our CASIMAC is closer to the diagonal reference line than the curves of the other classifiers. In particular, the GPC curve takes on a sigmoidal shape with major deviations from the diagonal at the beginning and the end. In order to obtain a quantitative measure for the observed miscalibrations, we calculate the corresponding area-deviation, i. e., the area between each curve and the reference line. In case of an optimal calibration, this area vanishes, otherwise it is positive. The results are listed in Table 4 and allow us to sort the classifiers: CASIMAC gives the by far best calibration result, followed by kNN and MLP with GPC at the very end.

Table 4: Calibration score measured in terms of the area-deviation (area between each curve and the reference line) for the calibration curves from Figure 6, which refer to the `pine` data set. The best result is highlighted in bold.

Score	CASIMAC	GPC	kNN	MLP
area-deviation	0.019	0.062	0.044	0.058

Summarized, our benchmark on different real-world data sets shows that our proposed CASIMAC can compete with other well-established classifiers and exhibits particularly good calibration properties.

3.3 Visualization

We outline in Section 2.4 how the latent space representation can be transformed onto a probability simplex for visualization purposes. In the following, we demonstrate this idea using the simplified data set `alcohol-3`, which is based on the data set `alcohol` from Table 2, but has three instead of five classes (i. e., $n = 3$, $d = 10$). We perform the class reduction by merging the last three classes into one.

Exemplarily, we train our classifier using $D = 25$ training data points so that there are $T = 100$ remaining test data points. We choose $\gamma = \frac{1}{2}$, $n_\alpha = 1$ and $n_\beta = 5$, Eqs. (7) and (19), with a 2-norm, Eq. (20), as distance metric, Eq. (9), and select the same GPR model as for the previous benchmarks; c. f. Appendix C.

The respective latent space visualization is shown in Figure 7. Specifically, we show the probability simplex \mathcal{S}^3 obtained from Eq. (17). In analogy to Figures 2 and 3 the probability simplex can be segmented into three congruent sectors according to the class probabilities.

The mapping of the training data is presented in Figure 7a in analogy to Figure 2a. By definition, Eq. (4), each training data point is mapped to the sector corresponding to its class. However, the distances to the neighboring classes can indicate inter-class relationships. We find that members of the classes 1 and 2 have a smaller distance to the border of class 3 than to their mutual border. Moreover, the closest distance between members of the classes 2 and 3 is exceedingly small.

The test data mapping in Figure 7b is performed according to the regression model, Eq. (11), in analogy to Figure 2b. Therefore, the test points can either be placed in the correct sector (in case of a correct prediction) or a wrong sector (in case of a wrong prediction). Hence, we can quantify the degree and direction of a misplaced data point according to its position in \mathcal{S}^3 . Interestingly, there is a misclassification between members of the classes 1 and 3, and particularly between members of the classes 2 and 3, but not between members of the classes 1 and 2 as one would expect from the previously discussed inter-class distances of the training data set. We list the detailed classification results of the test data set in form of a (transposed) confusion matrix in Table 5. As expected, most misclassifications happen between the classes 2 and 3.

Table 5: Confusion matrix (error matrix): class predictions versus true classes for each class. Each row of the matrix corresponds to a true class and each column to the number of estimates $\hat{y} = y$, Eq. (14), for its members. Correct classifications (on the diagonal) are highlighted in bold. There are no misclassifications between members of the classes 1 and 2 as indicated by Figure 7a.

True class	$\hat{y} = 1$	$\hat{y} = 2$	$\hat{y} = 3$
1 (20 members)	19	0	1
2 (20 members)	0	8	12
3 (60 members)	0	5	55

3.4 Towards Deep Learning

Finally, as a proof of concept for a classification task with a larger training data set, we consider the `fashion-mnist` data set, which consists of 28×28 pixel mages of fashion articles in 8-bit grayscale format (i. e., $\mathcal{X} \equiv \{0, \dots, 255\}^{784}$) as described in Xiao et al. (2017). In total, there are $D = 60\,000$ training images and $T = 10\,000$ test images, which are assigned to $n = 10$ classes. We perform a min-max normalization of the data so that the features lie within the range $[0, 1]$ before we feed it to our classifier.

For our classifier, we choose $\gamma = k_\beta = 1$, Eqs. (7b) and (19), and use a fully-connected neural network for the regression model, Eq. (11). The network contains a first hidden layer with 100 neurons and a sigmoid activation function and a second hidden layer with 18 neurons and a linear activation function. The output of the second layer is interpreted as the mean and standard deviation of a normal distribution. We optimize the log-likelihood of this distribution with an Adam approach to determine the best model parameters. In total, there are 80 318 trainable parameters. This model is realized with the help of Tensorflow-probability (Dillon et al., 2017). Since we predict a distribution for each input, we can calculate class probabilities according to Eq. (15).

For the latent space mapping, Eq. (4), we use two approaches. In the first approach we simply use the 2-norm, Eq. (20), as distance metric, Eq. (9). In the second approach, however, we take the average of three latent spaces

$$\mathbf{f}_{\text{effective}} \equiv \frac{\mathbf{f}_{\mathbf{d}_2} + \mathbf{f}_{\mathbf{d}_{\text{sim},5}} + \mathbf{f}_{\mathbf{d}_{\text{sim},13}}}{3}.$$

to obtain the effective latent space $\mathbf{f}_{\text{effective}}$. The first latent space component $\mathbf{f}_{\mathbf{d}_2}$ is based on the euclidean metric from the first approach, Eq. (20). The second and third latent space components $\mathbf{f}_{\mathbf{d}_{\text{sim},5}}$ and $\mathbf{f}_{\mathbf{d}_{\text{sim},13}}$ are based on the similarity metric

$$d_{\text{sim},w}(\mathbf{x}_1, \mathbf{x}_2) \equiv 1 - s_w(\mathbf{x}_1, \mathbf{x}_2)$$

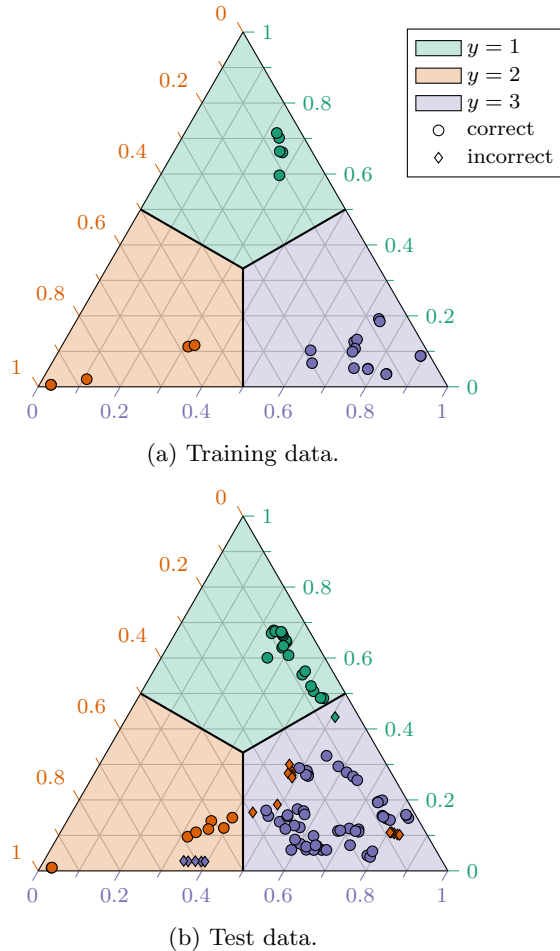


Figure 7: Probability simplex \mathcal{S}^3 for the `alcohol-3` data set ($n = 3$, $d = 10$), which can be used for the visualization of the latent space as described in Section 2.4. This probability simplex can be segmented into three congruent sectors (separated by —) according to the class probabilities. In (a) we show how the training data set is mapped to the simplex. The color of each point represents its true class. All training data is by definition correctly transformed into its corresponding sector. However, the distances indicate that members of the classes 1 and 2 are closer related to members of the class 3 than to each other. In (b) we show how the test data set is mapped to the simplex by the model. We distinguish between correctly mapped points (\circ) and incorrectly mapped points (\diamond). We find that there is a misclassification between members of the classes 1 and 3, and between members of the classes 2 and 3, but not between members of the classes 1 and 2, which exemplarily confirms the statement above about the inter-class relationships; c. f. Table 5.

with $w = 5$ and $w = 13$, respectively. Here, $s_w(\mathbf{x}_1, \mathbf{x}_2) \in [-1, 1]$ represents the structural similarity index for two images \mathbf{x}_1 and \mathbf{x}_2 with sliding window size w (Zhou Wang et al., 2004; Wang and Bovik, 2009) using the implementation from Van der Walt et al. (2014).

Summarized, our first approach with an euclidean metric can be considered *naive* since it does not take the structural properties of the images into account. On the other hand, the second approach is *informed* in the sense that it makes use of the fact that the data consists of images between which a structural relationship can be established.

The classification results are summarized in Table 6. Specifically, we show the top-1 to top-5 accuracy scores, which are based on the probability prediction of the classifier. It turns out that our informed approach is slightly better or equal to the naive approach for all accuracies. A list of benchmarked accuracies for other classifiers can be found, e. g., in Xiao et al. (2017).

Table 6: Top-1 to top-5 accuracy of our CASIMAC on the `fashion-mnist` data set. For the naive approach we use an euclidean distance metric between the images, whereas the informed approach also takes the structural image similarity into account. The best scores are highlighted in bold.

Accuracy	naive	informed
top-1	0.874	0.880
top-2	0.961	0.961
top-3	0.984	0.984
top-4	0.990	0.993
top-5	0.993	0.996

In contrast to the approach from Wilson et al. (2016), we use the neural network to directly perform the latent space mapping instead of linking the network to a series of GP. Furthermore, our network directly predicts the estimated mean and variance of the latent space mapping. It would, however, be a promising approach to further improve our results by incorporating such a more advanced form of feature extraction.

4 Conclusions and Outlook

In this paper, we have introduced a novel classifier called CASIMAC. It is based on the idea of transforming the classification problem into a well-defined regression problem. We achieve this by mapping the training data onto a simplex-like latent space. We have described in detail how our proposed algorithm works and have demonstrated that it can be successfully applied to real-world data sets from various fields. In particular, we see three major benefits of our approach.

First, it is generic in the sense that one can make use of arbitrary distance metrics and arbitrary regression models to perform the classification. This allows to inject additional expert knowledge into the classifier. For example, to classify molecules, a distance measure reflecting stoichiometry and configuration variations could be applied (Rupp et al., 2012). Such approaches can also be summarized under the term *informed learning* (von Rueden et al., 2020). Another strategy would be to infer the distance metric from the data itself, possibly based on certain informed assumptions (Bellet et al., 2013). Moreover, suitable distance metrics and models would also allow us to handle non-numerical features.

Second, our method is intuitive as the latent space representation has a direct interpretation and can even be used to visualize inter-class relationships. This is particularly useful for classification problems with a low number of classes and a high number of feature dimensions.

Third, our benchmarks have shown that our approach leads to well-calibrated predictions. To determine the class probabilities, we only require a regression model with an uncertainty estimate. In contrast to GPC, no complicated approximations are needed for this calculation. For a binary classification problem and a regression model with a normally distributed uncertainty, the class predictions can even be written in a closed form.

One challenge of our approach is the calculation of nearest neighbors, which is computationally expensive for larger data sets (Dhanabal and Chandramathi, 2011). It would be a promising starting point for further studies to show in how far this limitation can be overcome, e.g., by a suitable subsampling. Furthermore, the tuning of hyper-parameters can be costly. Instead of using a cross-validated grid search like we did in the paper, it could be more advantageous to consider a more elaborate strategy, e.g., to infer them from the statistical properties of the training data. We also consider this a possible point of origin for further research.

5 Acknowledgements

This work was developed in the Fraunhofer Cluster of Excellence “Cognitive Internet Technologies”. The authors would like to thank Janis Keuper and Jürgen Franke for their helpful and constructive comments.

A Proof of Simplex Sectioning

In the following, we briefly show that Eq. (10) allows a unique class reconstruction as stated in Section 2.1. This statement corresponds to Lemma 1. While it is clear for two dimensions (c. f. Figure 3), it is non-trivial for a higher-dimensional case. Here we use the abbreviation

$$\nu \equiv n - 1 \quad (22)$$

for reasons of convenience.

Lemma 1 (Distance relation for vertices of a regular simplex). *Suppose $\mathbf{p}_1, \dots, \mathbf{p}_{\nu+1}$ are the vertices of a regular ν -simplex in \mathbb{R}^ν with barycenter $\mathbf{0}$. Then, for every index $j = 1, \dots, \nu + 1$ and every real coefficient $c_1, \dots, c_{\nu+1} \geq 0$ the relation*

$$\arg \min_{k \in \{1, \dots, \nu+1\}} \left\| \sum_{\substack{i=1 \\ i \neq j}}^{\nu+1} c_i (-\mathbf{p}_i) - \mathbf{p}_k \right\|_2 = j \quad (23)$$

holds true.

Sketch of proof. By definition, the vertices fulfill Eq. (5). As a consequence, there is a common dihedral angle

$$\alpha = \arccos \left(-\frac{1}{\nu} \right) \quad (24)$$

between two different vertices as described in Parks and Wills (2002). Furthermore, we set j to a constant value. Based on these prerequisites, the proof requires three major steps.

First, we have to show that

$$\mathbf{S}_{j,k} \equiv \text{span} \{ \mathbf{p}_i : i = 1, \dots, \nu + 1 \text{ with } i \neq j, k \}$$

is the middle hyperplane of the line segment connecting \mathbf{p}_j and \mathbf{p}_k , i. e.,

$$\frac{\mathbf{p}_j + \mathbf{p}_k}{2} \in \mathbf{S}_{j,k} \wedge \mathbf{S}_{j,k} = \{ \mathbf{p}_{jk} \}^\perp \quad (25)$$

with

$$\mathbf{p}_{jk} \equiv \mathbf{p}_j - \mathbf{p}_k \quad (26)$$

for every $k \neq j$. Here we use $\text{span}\{\cdot\}$ to denote the linear span of a set of vectors and $\{\cdot\}^\perp$ stands for the orthogonal complement. The first part of Eq. (25) directly follows from Eq. (5a), whereas the second can be inferred from Eqs. (5) and (24).

Second, we have to show that the cone

$$\mathbf{C}_j \equiv \left\{ \mathbf{x} \in \mathbb{R}^\nu : \mathbf{x} = \sum_{\substack{i=1 \\ i \neq j}}^{\nu+1} d_i \mathbf{p}_i \text{ for some } d_1, \dots, d_{\nu+1} \geq 0 \right\} \quad (27)$$

is contained in the halfspace that is confined by the middle hyperplanes $\mathbf{S}_{j,k} \forall k \neq j$ and that points to the side of \mathbf{p}_j (instead of \mathbf{p}_k), i. e.,

$$\mathbf{C}_j \subset \bigcap_{\substack{k=1 \\ k \neq j}}^{\nu+1} [\mathbf{S}_{j,k} + \mathbf{P}_{jk}] \quad (28)$$

with

$$\mathbf{P}_{jk} \equiv \{ \mathbf{x} \in \mathbb{R}^\nu : \mathbf{x} = c \mathbf{p}_{jk} \text{ for some } c \geq 0 \}$$

for every $k \neq j$. Equation (28) follows from both parts of Eq. (25).

Third, we have to show that

$$\|\mathbf{x} - \mathbf{p}_j\|_2^2 \leq \|\mathbf{x} - \mathbf{p}_k\|_2^2 \forall \mathbf{x} \in \mathbf{S}_{j,k} + \mathbf{P}_{jk} \quad (29)$$

for every $k \neq j$. Again, Eq. (29) follows from Eq. (25).

Finally, we use the previously obtained results to complete the proof. Specifically, we define

$$\mathbf{x} \equiv \sum_{\substack{i=1 \\ i \neq j}}^{\nu+1} c_i(-\mathbf{p}_i)$$

so that

$$\mathbf{x} \in \mathbf{C}_j \subset \mathbf{S}_{j,k} + \mathbf{P}_{jk} \forall k \neq j$$

as a consequence of Eqs. (27) and (28). Using Eq. (29) we find

$$\|\mathbf{x} - \mathbf{p}_j\|_2^2 \leq \|\mathbf{x} - \mathbf{p}_k\|_2^2 \forall k \neq j$$

and hence arrive at the desired conclusion, Eq. (23). \square

B Implementation

A Python implementation of our proposed method is available online (Heese, 2020). The implementation includes the following main functionality, which is outlined in Algorithm 1:

- **TRAIN** (Line 1): Initial stage to determine the simplex vertices $\mathbf{P} \equiv \{\mathbf{p}_1, \dots, \mathbf{p}_n\}$ and to train the regression model \mathcal{M} based on a training data set \mathbf{D} , the user-defined parameters α , β , k_α and k_β , and the hyper-parameters \mathbf{m} of \mathcal{M} .
- **PREDICTLABEL** (Line 7): Predict the class labels of unseen data $\mathbf{x} \in \mathcal{X}$ based on the trained regression model \mathcal{M} and the simplex vertices \mathbf{P} .
- **PREDICTPROBABLITY** (Line 12): Predict the class probabilities of unseen data $\mathbf{x} \in \mathcal{X}$ based on the trained regression model \mathcal{M} and the simplex vertices \mathbf{P} .
- **DECISIONFUNCTION** (Line 24): Predict the binary decision function of unseen data $\mathbf{x} \in \mathcal{X}$ between two classes $j \in \mathcal{Y}$ and $k \in \mathcal{Y}$ based on the trained regression model \mathcal{M} and the simplex vertices \mathbf{P} .
- **TRANSFORM** (Line 29): Transform latent space coordinates $\mathbf{f} \in \mathcal{F}$ to probability simplex coordinates $\mathbf{s} \in \mathcal{S}^n$ based on the user-defined parameter τ and the simplex vertices \mathbf{P} .
- **INVERSETRANSFORM** (Line 33): Transform probability simplex coordinates $\mathbf{s} \in \mathcal{S}^n$ to latent space coordinates $\mathbf{f} \in \mathcal{F}$ based on the user-defined parameter τ and the simplex vertices \mathbf{P} .

We also show an overview of the functionality in Figure 8.

In particular, our implementation is intended to be used with scikit-learn (Pedregosa et al., 2011). Hence, we do not explicitly provide a regression model, Eq. (11), for step (t2) of the algorithm, but instead allow to plug in an arbitrary scikit-learn estimator. In the following, we briefly summarize important elements of our implementation.

B.1 Construction of Simplex Vectices

To obtain vertex coordinates of a regular ν -simplex centered at the origin for the latent space mapping from Section 2.1 (with the abbreviation ν from Eq. (22)), we first request that the vertices \mathbf{p}_i are unit vectors, i. e.,

$$\|\mathbf{p}_i\|_2 = 1 \forall i = 1, \dots, \nu + 1 \quad (30)$$

Algorithm 1 Main functionality of the provided implementation (Heese, 2020).

```

1: function TRAIN( $\mathbf{D}$ ,  $\alpha$ ,  $\beta$ ,  $k_\alpha$ ,  $k_\beta$ ,  $\mathbf{m}$ )
2:    $\mathbf{P} \equiv \{\mathbf{p}_1, \dots, \mathbf{p}_n\} \leftarrow$  Construct vertices using the method from Appendix B.1.
3:    $\mathbf{D}_F \leftarrow$  Calculate feature data set, Eq. (13), based on  $\tilde{\mathbf{f}}_{\alpha, \beta, k_\alpha, k_\beta}$ , Eq. (32), with  $\mathbf{D}$  and  $\mathbf{P}$ .
4:    $\mathcal{M} \leftarrow$  Train regression model based on  $\mathbf{D}_F$  and the model hyper-parameters  $\mathbf{m}$ .
5:   return  $\mathcal{M}$ ,  $\mathbf{P}$ 
6: end function
7: function PREDICTLABEL( $\mathbf{x}$ ,  $\mathcal{M}$ ,  $\mathbf{P}$ )
8:    $\hat{\mathbf{f}} \leftarrow$  Predict  $\hat{\mathbf{f}}(\mathbf{x}|\mathbf{D})$  using  $\mathcal{M}$ .
9:    $y \leftarrow$  Reconstruct class  $y(\hat{\mathbf{f}})$  using Eq. (10) with  $\mathbf{P}$ .
10:  return  $y$ 
11: end function
12: function PREDICTPROBABLITY( $\mathbf{x}$ ,  $\mathcal{M}$ ,  $\mathbf{P}$ )
13:   $\hat{\boldsymbol{\mu}}, \hat{\boldsymbol{\sigma}} \leftarrow$  Predict  $\hat{\boldsymbol{\mu}}(\mathbf{D}, \mathbf{x})$  and  $\hat{\boldsymbol{\sigma}}(\mathbf{D}, \mathbf{x})$  using  $\mathcal{M}$ , Eq. (35).
14:  if  $n = 2$  then ▷ Analytically closed form.
15:     $\hat{p}_\mu \leftarrow$  Calculate class probability using Eq. (36).
16:     $\hat{p}_\sigma \leftarrow 0$ 
17:  else ▷ Monte-Carlo approach.
18:     $\mathbf{f}_1, \dots, \mathbf{f}_N \leftarrow$  Draw samples using Eq. (37).
19:     $\hat{p}_\mu \leftarrow$  Calculate class probability using Eq. (38) with  $\mathbf{f}_1, \dots, \mathbf{f}_N$  and  $\mathbf{P}$ .
20:     $\hat{p}_\sigma \leftarrow$  Calculate standard deviation using Eq. (39) with  $\mathbf{f}_1, \dots, \mathbf{f}_N$ .
21:  end if
22:  return  $\hat{p}_\mu, \hat{p}_\sigma$ 
23: end function
24: function DECISIONFUNCTION( $\mathbf{x}$ ,  $\mathcal{M}$ ,  $\mathbf{P}$ ,  $j$ ,  $k$ )
25:   $\hat{\boldsymbol{\mu}} \leftarrow$  Predict  $\hat{\boldsymbol{\mu}}(\mathbf{D}, \mathbf{x})$  using  $\mathcal{M}$ , Eq. (35).
26:   $\delta_{jk} \leftarrow$  Calculate binary decision function using Eq. (40) with  $\mathbf{P}$ .
27:  return  $\delta_{jk}$ 
28: end function
29: function TRANSFORM( $\mathbf{f}$ ,  $\tau$ ,  $\mathbf{P}$ )
30:   $\mathbf{s} \leftarrow$  Perform transformation  $\mathbf{S}_\tau(\mathbf{f})$  using Eq. (41) with  $\tau$  and  $\mathbf{P}$ .
31:  return  $\mathbf{s}$ 
32: end function
33: function INVERSETRANSFORM( $\mathbf{s}$ ,  $\tau$ ,  $\mathbf{P}$ )
34:   $\mathbf{f} \leftarrow$  Perform transformation  $\mathbf{S}_\tau^{-1}(\mathbf{s})$  using Eq. (42) with  $\tau$  and  $\mathbf{P}$ .
35:  return  $\mathbf{f}$ 
36: end function

```

in accordance with Eq. (5b). Together with Eq. (24) this assumption leads to the expression

$$\mathbf{p}_i \cdot \mathbf{p}_j = \begin{cases} 1 & \text{if } i = j \\ -\frac{1}{\nu} & \text{else} \end{cases} \quad \forall i, j = 1, \dots, \nu + 1 \quad (31)$$

for the scalar products between the vertices.

Second, we set $\mathbf{p}_1 = (1, 0, \dots, 0)^\top$ without loss of generality. The remaining vertices $\mathbf{p}_2, \dots, \mathbf{p}_\nu$ can then be found by iterating over each row of the $(\nu) \times (\nu + 1)$ vertex matrix $(\mathbf{p}_1, \dots, \mathbf{p}_{\nu+1})$ and using the conditions Eqs. (30) and (31) under the constraint

$$\|\mathbf{p}_i\|_0 = \begin{cases} i & \text{if } i < \nu \\ \nu & \text{else} \end{cases} \quad \forall i = 1, \dots, \nu + 1$$

to specify the remaining coordinates. Here $\|\cdot\|_0$ denotes the 0-norm (corresponding to the number of non-zero components).

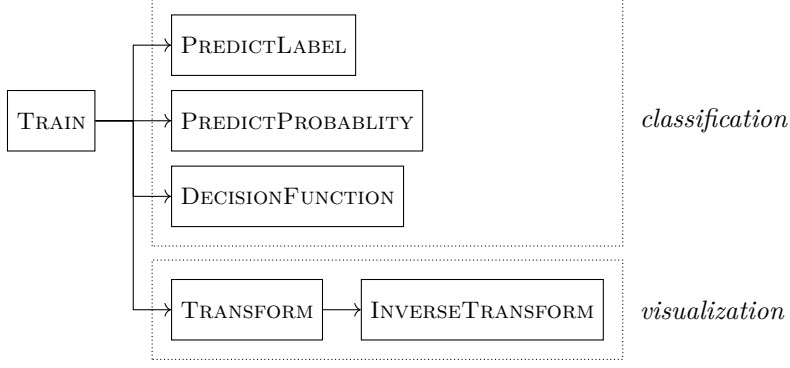


Figure 8: Overview of the functionality of the provided implementation (Heese, 2020) as outlined in Algorithm 1. After the initial training stage, there are two possible use cases, namely classification and visualization, as described in more detail in Section 2. The first use case refers to the prediction of class labels, class probabilities and binary decision functions of unseen data, whereas the second use case allows to perform a transformation from the latent space to a corresponding probability simplex and back for visualization purposes.

This approach leads to a set of vertices fulfilling Eq. (5). In particular, such a set is unique apart from joint rotations.

B.2 Generalized Latent Space Mapping

Our implementation provides a slight generalization of the latent space mapping defined in Eq. (4). This generalized approach allows to specify additional transformations to the attraction and repulsion terms, which might be suitable for certain applications. Specifically, we propose

$$\tilde{\mathbf{f}}_{\alpha,\beta,k_\alpha,k_\beta}(\mathbf{D}, \mathbf{x}, y) \equiv \sum_{\substack{y'=1 \\ y' \neq y}}^n \left[\tilde{f}_C(\tilde{C}_{\alpha,\beta,k_\alpha,k_\beta}(\mathbf{D}, \mathbf{x}, y, y')) \cdot (-\mathbf{p}_{\mathbf{y}'}) \right] \quad (32)$$

with

$$\begin{aligned} \tilde{C}_{\alpha,\beta,k_\alpha,k_\beta}(\mathbf{D}, \mathbf{x}, y, y') &\equiv \alpha \cdot \tilde{f}_A(\Upsilon_{k_\alpha}[\{\mathbf{x}' \in \mathbf{X}(\mathbf{D}, y) : d(\mathbf{x}, \mathbf{x}') > 0\}]) \\ &+ \beta \cdot \tilde{f}_R(\Upsilon_{k_\beta}[\mathbf{X}(\mathbf{D}, y')]) \end{aligned} \quad (33)$$

based on arbitrary user-defined functions

$$\tilde{f}_A : \mathbf{X}' \mapsto \mathbb{R}_{\geq 0}$$

and

$$\tilde{f}_R : \mathbf{X}' \mapsto \mathbb{R}_{\geq 0}$$

with $\mathbf{X}' \subseteq \mathbf{X}(\mathbf{D}, y)$ as well as

$$\tilde{f}_C : \mathbb{R}_{\geq 0} \mapsto \mathbb{R}_{\geq 0}.$$

In Eq. (33) we made use of the set of k nearest neighbors

$$\Upsilon_k[\mathbf{X}] \equiv \left\{ \mathbf{x}' \in \mathbf{X}' : \mathbf{X}' = \arg \min_{\substack{\mathbf{X}' \subseteq \mathbf{X} \\ |\mathbf{X}'|=k}} \sum_{\mathbf{x}' \in \mathbf{X}'} d(\mathbf{x}, \mathbf{x}') \right\}$$

defined in analogy to the mean distance of the nearest neighbors, Eq. (8). By choosing \tilde{f}_R as the mapping to Eq. (8), \tilde{f}_A as the mapping to the multiplicative inverse of Eq. (8), and \tilde{f}_C as the identity map, we arrive at Eq. (4).

B.3 Class Probability Calculation

Generally, the estimated probability $\hat{p}(y|\mathbf{D}, \mathbf{x})$ is defined by Eq. (15). In our implementation we assume that $\hat{p}(\mathbf{f}|\mathbf{D}, \mathbf{x})$ has the form of a normal distribution, i. e.,

$$\hat{p}(\mathbf{f}|\mathbf{D}, \mathbf{x}) = \mathcal{N}(\hat{\boldsymbol{\mu}}, \hat{\boldsymbol{\sigma}}) \equiv \frac{\exp\left[-\frac{1}{2}(\mathbf{f} - \hat{\boldsymbol{\mu}})^\top \hat{\boldsymbol{\sigma}}^{-1}(\mathbf{f} - \hat{\boldsymbol{\mu}})\right]}{\sqrt{(2\pi)^{(n-1)} \det(\hat{\boldsymbol{\sigma}})}} \quad (35)$$

with mean $\hat{\boldsymbol{\mu}} \equiv \hat{\boldsymbol{\mu}}(\mathbf{D}, \mathbf{x}) \in \mathbb{R}^{n-1}$ and covariance $\hat{\boldsymbol{\sigma}} \equiv \hat{\boldsymbol{\sigma}}(\mathbf{D}, \mathbf{x}) \in \mathbb{R}^{(n-1) \times (n-1)}$, respectively.

Consequently, for $n = 2$ we arrive at the closed form

$$\hat{p}(y = 1|\mathbf{D}, \mathbf{x}) = \frac{1}{2} \left(1 + \operatorname{erf} \left[\frac{|\hat{\mu}|}{\sqrt{2}\hat{\sigma}} \right] \right) = 1 - \hat{p}(y = 2|\mathbf{D}, \mathbf{x}) \quad (36)$$

using the notation $\hat{\mu} \equiv \hat{\boldsymbol{\mu}}$ and $\hat{\sigma}^2 \equiv \hat{\boldsymbol{\sigma}}$ for the scalar mean and variance, respectively.

For $n > 2$ we use a Monte-Carlo importance sampling (Srinivasan, 2002), where we draw N samples

$$\mathbf{f}_1, \dots, \mathbf{f}_N \sim \mathcal{N}(\hat{\boldsymbol{\mu}}, \hat{\boldsymbol{\sigma}}). \quad (37)$$

Thus,

$$\hat{p}(y|\mathbf{D}, \mathbf{x}) \approx \hat{p}_\mu \pm \hat{p}_\sigma$$

with the expectation value

$$\hat{p}_\mu \equiv \hat{p}_\mu(y; \mathbf{f}_1, \dots, \mathbf{f}_N) \equiv \frac{1}{N} \sum_{i=1}^N \mathbb{1}(y, \mathbf{f}_i) \in [0, 1] \quad (38)$$

and the best estimate for its standard deviation

$$\hat{p}_\sigma \equiv \hat{p}_\sigma(y; \mathbf{f}_1, \dots, \mathbf{f}_N) \approx \sqrt{\frac{\hat{p}_\mu^2(1 - \hat{p}_\mu) + \hat{p}_\mu(1 - \hat{p}_\mu)^2}{N - 1}}, \quad (39)$$

where we have recalled the indicator function $\mathbb{1}(y, \mathbf{f})$, Eq. (16).

Our implementation is limited to diagonal covariance matrices $\hat{\boldsymbol{\sigma}}$, but an analogous approach can in principle also be used for non-diagonal covariance matrices or non-normal probability distributions. Furthermore, our implementation additionally provides analytic gradients for Eq. (36) with respect to the features if the regression model also provides such gradients for its predictions.

B.4 Binary Decision Function

The binary decision function provides an alternative, non-probabilistic metric to determine the degree of membership of $\mathbf{x} \in \mathcal{X}$ to a particular pair of classes by projecting a latent vector orthogonal to segmenting planes. It is defined pair-wise between two classes $j \in \mathcal{Y}$ and $k \in \mathcal{Y}$ as

$$\boldsymbol{\delta}_{jk}(\mathbf{D}, \mathbf{x}) \equiv \frac{\hat{\boldsymbol{\mu}} \cdot \mathbf{p}_{jk}}{\|\mathbf{p}_{jk}\|_2}, \quad (40)$$

where we have recalled $\hat{\boldsymbol{\mu}}$ from Appendix B.3 and \mathbf{p}_{jk} from Eq. (26). The binary decision function indicates membership to class j for $\boldsymbol{\delta}_{jk}(\mathbf{D}, \mathbf{x}) > 0$ and membership to class k for $\boldsymbol{\delta}_{jk}(\mathbf{D}, \mathbf{x}) < 0$ with respect to these two classes only (while ignoring the membership to other classes due to the projection). The case $\boldsymbol{\delta}_{jk}(\mathbf{D}, \mathbf{x}) = 0$ corresponds to the binary decision border between the two classes.

In analogy to Eq. (36), our implementation provides analytic gradients for Eq. (40) with respect to the features if the regression model also provides such gradients for its predictions.

B.5 Probability Simplex Transformation

To define the bijective transformation from Eq. (17) we consider an arbitrary latent vector $\mathbf{f} \in \mathbb{R}^\nu$ and a set of simplex vertices $\mathbf{p}_1, \dots, \mathbf{p}_{\nu+1}$, which have been constructed according to Appendix B.1. Again, we make use of the abbreviation ν from Eq. (22).

Specifically,

$$\mathbf{S}_\tau(\mathbf{f}) \equiv \frac{\sum_{i=1}^{\nu+1} \exp[\tau \mathbf{f} \cdot \mathbf{p}_i] \mathbf{e}_i}{\sum_{i=1}^{\nu+1} \exp[\tau \mathbf{f} \cdot \mathbf{p}_i]} \quad (41)$$

maps from \mathbb{R}^ν to the $(\nu + 1)$ -dimensional probability simplex

$$\mathcal{S}^{(\nu+1)} \equiv \left\{ \mathbf{s} \in \mathbb{R}^{\nu+1} : \mathbf{s} = \sum_{i=1}^{\nu+1} s_i \mathbf{e}_i \text{ for some } s_1, \dots, s_{\nu+1} \geq 0 \wedge \sum_{i=1}^{\nu+1} s_i = 1 \right\}$$

for any $\tau \in \mathbb{R}_{\neq 0}$. Here, $\mathbf{e}_1, \dots, \mathbf{e}_{\nu+1}$ denote the natural basis of $\mathbb{R}^{\nu+1}$.

The inverse transformation of Eq. (41) reads

$$\mathbf{S}_\tau^{-1}(\mathbf{s}) \equiv \frac{\nu \sum_{i=1}^{\nu+1} \ln[\mathbf{s} \cdot \mathbf{e}_i] \mathbf{p}_i}{\tau(\nu + 1)} \quad (42)$$

for any $\mathbf{s} \in \mathbb{R}^{\nu+1}$. Indeed, it can be straightforwardly shown that

$$\mathbf{S}_\tau^{-1}(\mathbf{S}_\tau(\mathbf{f})) = \mathbf{f}$$

for any $\mathbf{f} \in \mathbb{R}^\nu$ by inserting the equations and making use of Eqs. (5a) and (31) and the orthonormality of $\mathbf{e}_1, \dots, \mathbf{e}_{\nu+1}$. The verification of

$$\mathbf{S}_\tau(\mathbf{S}_\tau^{-1}(\mathbf{s})) = \mathbf{s}$$

for any $\mathbf{s} \in \mathcal{S}^{(\nu+1)}$ can be performed in an analogous way.

The user-defined scaling factor τ can be chosen arbitrary but equal in Eqs. (41) and (42). For convenience we propose the data-dependent rescaling

$$\tau = \tau_\sigma(\mathbf{D}_\mathbf{F}) \equiv \frac{1}{\min_i \sigma_i(\mathbf{D}_\mathbf{F})} > 0,$$

where $\sigma_i(\mathbf{D}_\mathbf{F})$ represents the standard deviation of the i th component of the features $\mathbf{f} \in \mathbf{D}_\mathbf{F}$, Eq. (13).

C Benchmark

In Section 3 we use cross-validation to select the best hyper-parameters for the classifiers out of a predefined set of possible choices. Specifically, we vary the number of nearest neighbors $k \in \{5, 10, 15, 20\}$ for kNN, the hidden layer sizes $L \in \{(5), (10), (5, 5), (5, 10), (10, 10), (5, 5, 5), (5, 5, 10), (5, 10, 10), (10, 10, 10)\}$ (all with a ReLU activation function) for MLP and the kernel parameters for both GPC and the GPR model used for CASIMAC. For these kernels we choose a sum of a Matern kernel and a white noise kernel (Rasmussen and Williams, 2006) and tune the Matern coefficient $\nu \in \{\frac{3}{2}, \frac{5}{2}, \infty\}$. The remaining kernel parameters are optimized for each cross-validation setup as described in Rasmussen and Williams (2006). Additionally, for CASIMAC, we tune both γ , Eqs. (7) and (19), as well as k_α and k_β , Eq. (7).

In Table 7 we list the cross-validated hyper-parameters, which result in the best accuracy over all classification tasks for each data set from Section 3.2. Analogously, for the artificial data set from Section 3.1 we get the best hyper-parameters $\gamma = 1$, $k_\alpha = 10$, $k_\beta = 10$, and $\nu = \infty$ for CASIMAC and $\nu = \frac{3}{2}$ for GPC. Finally, for the `alcohol-3` data set from Section 3.3 $\gamma = \frac{1}{2}$, $k_\alpha = 1$, and $k_\beta = 5$ are fixed and we find $\nu = \infty$ for CASIMAC from the cross-validation.

Table 7: Best cross-validated hyper-parameters for the real-world data sets from Table 2.

alcohol	climate	hiv	pine	wifi
CASIMAC				
$\gamma = 0$ $k_\alpha = 5$ $k_\beta = 5$ $\nu = \infty$	$\gamma = 0$ $k_\alpha = 5$ $k_\beta = 5$ $\nu = \infty$	$\gamma = 0$ $k_\alpha = 20$ $k_\beta = 20$ $\nu = \frac{3}{2}$	$\gamma = 1$ $k_\alpha = 1$ $k_\beta = 5$ $\nu = \frac{3}{2}$	$\gamma = 1/3$ $k_\alpha = 20$ $k_\beta = 20$ $\nu = \infty$
GPC				
$\nu = \frac{3}{2}$	$\nu = \frac{3}{2}$	$\nu = \infty$	$\nu = \frac{3}{2}$	$\nu = \frac{3}{2}$
kNN				
$k = 5$	$k = 5$	$k = 5$	$k = 5$	$k = 5$
MLP				
$L =$ (10, 10, 10)	$L =$ (5, 5)	$L =$ (5, 10)	$L =$ (10, 10, 10)	$L =$ (5, 5)

References

- Adak MF, Lieberzeit P, Jarujamrus P, Yumusak N (2019) Classification of alcohols obtained by QCM sensors with different characteristics using abc based neural network. Engineering Science and Technology, an International Journal
- Al-Shedivat M, Wilson AG, Saatchi Y, Hu Z, Xing EP (2017) Learning scalable deep kernels with recurrent structure. The Journal of Machine Learning Research 18(1):2850–2886
- Baumgardner MF, Biehl LL, Landgrebe DA (2015) 220 Band AVIRIS Hyperspectral Image Data Set: June 12, 1992 Indian Pine Test Site 3. Available online: <https://purr.purdue.edu/publications/1947/1>
- Bellet A, Habrard A, Sebban M (2013) A survey on metric learning for feature vectors and structured data. preprint arXiv:13066709 (<http://arxiv.org/abs/1306.6709>)
- Boyd S, Vandenberghe L (2004) Convex Optimization. Cambridge University Press
- Bradshaw J, Matthews AG, Ghahramani Z (2017) Adversarial examples, uncertainty, and transfer testing robustness in Gaussian process hybrid deep networks. preprint arXiv:170702476 (<http://arxiv.org/abs/1707.02476>)
- Calandra R, Peters J, Rasmussen CE, Deisenroth MP (2016) Manifold Gaussian processes for regression. In: International Joint Conference on Neural Networks, IEEE, IJCNN '16, pp 3338–3345
- Challis E, Hurley P, Serra L, Bozzali M, Oliver S, Cercignani M (2015) Gaussian process classification of Alzheimer’s disease and mild cognitive impairment from resting-state fMRI. NeuroImage 112:232–243
- Coxeter HSM (1973) Regular Polytopes. Dover books on advanced mathematics, Dover, New York
- Cremanns K, Roos D (2017) Deep Gaussian covariance network. preprint arXiv:171006202 (<http://arxiv.org/abs/1710.06202>)
- Daskalakis C, Dellaportas P, Panos A (2020) Scalable gaussian processes, with guarantees: Kernel approximations and deep feature extraction. preprint arXiv:200401584 (<http://arxiv.org/abs/2004.01584>)
- DeGroot MH, Fienberg SE (1983) The comparison and evaluation of forecasters. Journal of the Royal Statistical Society Series D (The Statistician) 32(1/2):12–22
- Deza MM, Deza E (2016) Encyclopedia of Distances. Springer, Berlin

- Dhanabal S, Chandramathi DS (2011) A review of various k-nearest neighbor query processing techniques. *International Journal of Computer Applications* 31(7):14–22
- Dillon JV, Langmore I, Tran D, Brevdo E, Vasudevan S, Moore D, Patton B, Alemi A, Hoffman MD, Saurous RA (2017) TensorFlow distributions. preprint arXiv:1711.10604 abs/1711.10604, (<http://arxiv.org/abs/1711.10604>)
- Dua D, Graff C (2017) UCI machine learning repository. Available online: <http://archive.ics.uci.edu/ml>
- GPY (2012) GPY: A Gaussian process framework in Python. Available online: <http://github.com/SheffieldML/GPY>
- Graña M, M A Veganzons BA (2014) Hyperspectral remote sensing scenes. Available online: http://www.ehu.es/ccwintco/index.php/Hyperspectral_Remote_Sensing_Scenes
- Heese R (2020) CASIMAC: Calibrated simplex mapping classifier in Python. Available online: <https://github.com/raoulheese/casimac>
- Hensman J, Matthews AG, Filippone M, Ghahramani Z (2015) MCMC for variationally sparse Gaussian processes. In: Cortes C, Lawrence ND, Lee DD, Sugiyama M, Garnett R (eds) *Advances in Neural Information Processing Systems* 28, Curran Associates, Inc., pp 1648–1656
- Iwata T, Ghahramani Z (2017) Improving output uncertainty estimation and generalization in deep learning via neural network Gaussian processes. preprint arXiv:1707.05922 (<http://arxiv.org/abs/1707.05922v1>)
- Liu H, Ong YS, Shen X, Cai J (2018) When Gaussian process meets big data: A review of scalable GPs. preprint arXiv:1807.01065 (<http://arxiv.org/abs/1807.01065>)
- Lucas DD, Klein R, Tannahill J, Ivanova D, Brandon S, Domyancic D, Zhang Y (2013) Failure analysis of parameter-induced simulation crashes in climate models. *Geoscientific Model Development* 6(4):1157–1171
- Ludl P, Heese R, Höller J, Asprión N, Bortz M (2021) Using machine learning models to explore the solution space of large non-linear systems underlying flowsheet simulations with constraints, submitted to *Frontiers of Chemical Science and Engineering*
- Niculescu-Mizil A, Caruana R (2005) Predicting good probabilities with supervised learning. In: *International Conference on Machine Learning*, ACM, New York, NY, USA, ICML '05, pp 625–632
- Opitz J, Burst S (2019) Macro F1 and Macro F1. preprint arXiv:1911.03347 (<http://arxiv.org/abs/1911.03347>)
- Parks HR, Wills DC (2002) An elementary calculation of the dihedral angle of the regular n-simplex. *The American Mathematical Monthly* 109(8):756–758
- Pedregosa F, Varoquaux G, Gramfort A, Michel V, Thirion B, Grisel O, Blondel M, Prettenhofer P, Weiss R, Dubourg V, Vanderplas J, Passos A, Cournapeau D, Brucher M, Perrot M, Duchesnay E (2011) Scikit-learn: Machine learning in Python. *Journal of Machine Learning Research* 12:2825–2830
- Platt J (2000) Probabilistic outputs for support vector machines and comparisons to regularized likelihood methods. *Advances in Large Margin Classifiers* 10
- Rasmussen CE, Williams CKI (2006) *Gaussian Processes for Machine Learning*. Adaptive computation and machine learning series, University Press Group Limited
- Rögnvaldsson T, You L, Garwicz D (2014) State of the art prediction of HIV-1 protease cleavage sites. *Bioinformatics* 31(8):1204–1210
- Rohra JG, Perumal B, Narayanan SJ, Thakur P, Bhatt RB (2016) User localization in an indoor environment using fuzzy hybrid of particle swarm optimization & gravitational search algorithm with neural networks. In: *International Conference on Soft Computing for Problem Solving*, SocProS '16

- von Rueden L, Mayer S, Beckh K, Georgiev B, Giesselbach S, Heese R, Kirsch B, Pfrommer J, Pick A, Ramamurthy R, Walczak M, Garcke J, Bauckhage C, Schuecker J (2020) Informed machine learning – a taxonomy and survey of integrating knowledge into learning systems. preprint arXiv:1903.12394 (<https://arxiv.org/abs/1903.12394>)
- Rupp M, Tkatchenko A, Müller KR, Von Lilienfeld OA (2012) Fast and accurate modeling of molecular atomization energies with machine learning. *Physical review letters* 108(5):058301
- Srinivasan R (2002) *Importance Sampling: Applications in Communications and Detection*. Springer, Berlin
- Tran D, Ranganath R, Blei DM (2015) The variational Gaussian process. preprint arXiv:1511.06499 (<http://arxiv.org/abs/1511.06499>)
- Van Der Maaten L, Postma E, Van den Herik J (2009) Dimensionality reduction: a comparative review. Tech. Rep. TiCC TR 2009–005, Tilburg University
- Van der Walt S, Schönberger JL, Nunez-Iglesias J, Boulogne F, Warner JD, Yager N, Goullart E, Yu T (2014) scikit-image: image processing in Python. *PeerJ* 2:e453
- Wang Z, Bovik AC (2009) Mean squared error: Love it or leave it? A new look at signal fidelity measures. *IEEE Signal Processing Magazine* 26(1):98–117
- Wilson AG, Hu Z, Salakhutdinov RR, Xing EP (2016) Stochastic variational deep kernel learning. In: *Advances in Neural Information Processing Systems*, pp 2586–2594
- Xiao H, Rasul K, Vollgraf R (2017) Fashion-MNIST: a novel image dataset for benchmarking machine learning algorithms. preprint arXiv:1708.07747 (<http://arxiv.org/abs/1708.07747>)
- Zadrozny B, Elkan C (2002) Transforming classifier scores into accurate multiclass probability estimates. In: *International Conference on Knowledge Discovery and Data Mining*, ACM, New York, NY, USA, KDD '02, pp 694–699
- Zhou Wang, Bovik AC, Sheikh HR, Simoncelli EP (2004) Image quality assessment: from error visibility to structural similarity. *IEEE Transactions on Image Processing* 13(4):600–612